Imaging the mechanisms of anti-CD20 therapy in vivo uncovers spatiotemporal bottlenecks in antibody-dependent phagocytosis

Capucine Grandjean, Zacarias Garcia, Fabrice Lemaître, Béatrice Bréart, Philippe Bousso

To cite this version:

Capucine Grandjean, Zacarias Garcia, Fabrice Lemaître, Béatrice Bréart, Philippe Bousso. Imaging the mechanisms of anti-CD20 therapy in vivo uncovers spatiotemporal bottlenecks in antibody-dependent phagocytosis. Science Advances , 2021, 7 (8), pp.eabd6167. ⟨10.1126/sciadv.abd6167⟩. ⟨hal-03231367⟩

HAL Id: hal-03231367
https://hal.science/hal-03231367v1

Submitted on 25 May 2021

IMMUNOLOGY

Imaging the mechanisms of anti-CD20 therapy in vivo uncovers spatiotemporal bottlenecks in antibody-dependent phagocytosis

Capucine L. Grandjean[1,2]*, Zacarias Garcia[1,2], Fabrice Lemaître[1,2], Béatrice Bréart[1,2], Philippe Bousso[1,2]*

Anti-CD20 antibody (mAb) represents an effective strategy for the treatment of B cell malignancies, possibly involving complement activity, antibody-dependent cellular cytotoxicity and phagocytosis (ADP). While ADP by Kupffer cells deplete circulating tumors, mechanisms targeting non-circulating tumors remain unclear. Using intravital imaging in a model of B cell lymphoma, we establish here the dominance and limitations of ADP in the bone marrow (BM). We found that tumor cells were stably residing in the BM with little evidence for recirculation. To elucidate the mechanism of depletion, we designed a dual fluorescent reporter to visualize phagocytosis and apoptosis. ADP by BM-associated macrophages was the primary mode of tumor elimination but was no longer active after one hour, resulting in partial depletion. Moreover, macrophages were present at low density in tumor-rich regions, targeting only neighboring tumors. Overcoming spatiotemporal bottlenecks in tumor-targeting Ab therapy thus represents a critical path towards the design of optimized therapies.

INTRODUCTION

Monoclonal antibodies (mAbs) targeting tumor surface antigen represent a powerful strategy for the treatment of several types of cancer. Rituximab, a chimeric immunoglobulin G1 (IgG1) mAb directed against the CD20 molecule, was the first approved antitumor therapeutic mAb and has since improved the prognosis of patients with various B cell malignancies (*1*). Anti-CD20 therapy is now also widely used to treat several autoimmune diseases (*1*–*3*).

Anti-CD20 mAb acts by depleting normal and malignant B cells, and multiple studies have provided clues about its mode of action. In vitro studies indicated that anti-CD20 mAb can trigger complement-dependent cytotoxicity (*4*–*7*), a mechanism possibly favored by the structure of CD20 clustering (*8*) by the mAb. Because Ab-dependent cellular cytotoxicity (ADCC) by natural killer (NK) cells has been readily observed in vitro, it has often been considered to be the main mechanism of tumor depletion by therapeutic Abs (*1*, *9*–*12*). Notably, Ab-dependent phagocytosis (ADP) by macrophages has also been frequently observed in vitro and was reported to be more efficient than ADCC on a per-cell basis (*13*). Preclinical models have strongly supported the role of FcR-dependent mechanisms for antitumor activity (*3*, *14*–*23*). In addition, depletion of macrophages/monocytes in these models has supported their essential role in mediating mAb therapeutic activity (*14*, *15*, *17*, *20*, *24*, *25*). Other studies have pointed toward an important role of neutrophils in therapeutic mAb antitumor activity (*26*–*28*). In cancer patients, polymorphisms in Fc receptors have been associated with improved therapeutic response to mAb, further supporting the role of Fc-dependent mechanisms in vivo (*29*–*32*). However, despite two decades of clinical use, the respective contribution of each of these mechanisms to the therapeutic response of anti-CD20 mAb has not been fully understood (*1*).

As an additional degree of complexity, the mode of action of therapeutic mAb can also vary with the anatomical site. For example, Ly6C^{high} monocyte-derived cells or resident macrophages were found to be the main effectors during mAb treatment of tumors located in the skin and lung, respectively (*20*). Moreover, distinct contributions for Fc receptors and the complement pathway have been observed in the spleen versus the bone marrow (BM) in a model of mAb-mediated cell depletion (*25*). Last, the liver is also an important site for therapeutic activity, as we and others have shown that Kupffer cells are essential to deplete circulating malignant targets in response to mAb (*17*, *18*, *24*). However, in the context of B cell malignancies, many tumor cells may not have the ability to reach the circulation to be targeted by Kupffer cells, raising the question of putative mechanisms acting in tumor-infiltrated lymphoid organs.

Anti-CD20 therapy also exhibits some limitations. While anti-CD20 mAb has contributed to increase patient survival in distinct types of B cell lymphomas, it is most often not curative (*1*). A large proportion of patients ultimately relapses, and several mechanisms of resistance have been identified (*5*, *11*, *33*–*37*). Preclinical models have shown, in particular, that the BM is a niche for low therapeutic immunoglobulin G (IgG) activity (*25*, *38*, *39*). Strategies to circumvent these limitations included Ab glycoengineering (*18*, *40*–*42*) and combination with chemotherapy (*39*) or with phagocytosis checkpoints (*43*, *44*) including anti-CD47 or anti-CD24 Abs (*26*, *45*, *46*).

Together, these observations highlight the importance of identifying the bottlenecks in anti-CD20 Ab therapy. Here, we combined intravital imaging and a fluorescent dual reporter for phagocytosis and apoptosis to characterize the mechanisms and dynamics of anti-CD20 mAb antitumor activity in the BM of B cell lymphoma–bearing mice. We found that ADP by BM-associated macrophages plays a dominant role in tumor cell elimination. Both temporal and spatial constraints limited the extent of ADP, raising important considerations for treatment optimization.

---

[1] Dynamics of Immune Responses Unit, Equipe Labellisée Ligue Contre le Cancer, Institut Pasteur, 75015 Paris, France. [2] INSERM U1223, 75015 Paris, France.
*Corresponding author. Email: capucine.grandjean@pasteur.fr (C.L.G.); philippe.bousso@pasteur.fr (P.B.)

RESULTS

B cell tumors reside stably in the BM

To study the dynamics of anti-CD20 therapy in a tumor setting, we relied on a mouse model of Burkitt-like B cell lymphoma. We isolated B cell tumors from Eμ-myc mice (*47*) that develop spontaneous B cell lymphomas. Tumors isolated from distinct animals were found to express variable levels of CD20 (fig. S1). To ensure that CD20 expression was not limiting in our model, we generated by retroviral transduction a B cell tumor cell line expressing high levels of CD20 (in the same range as endogenous B cells in vivo) together with a fluorescent protein (Fig. 1A and fig. S2). When injected in immunocompetent recipients, tumors established primarily in the BM (Fig. 1B) and were also detected (often at later times) in other organs (*48*). In addition, a fraction of tumor cells was found circulating in the blood (Fig. 1B). Previous studies have demonstrated that circulating tumors are eliminated by Kupffer cells during mAb therapy (*17*, *18*, *24*). However, the dynamics and fate of B cell tumors residing in lymphoid organs such as the BM are yet to be fully characterized. To address this question, we used intravital two-photon imaging focusing on the BM and the liver, a site where tumor cell recirculation can be readily observed (*17*, *24*). As expected, a substantial fraction of tumor cells was found rapidly circulating in the liver sinusoids, while others were sparsely distributed in the liver parenchyma (Fig. 1C and movie S1). By contrast, tumors grew at high-density forming clusters in the BM, with the vast majority being sessile and showing little evidence for recirculation (Fig. 1C and movie S2). Thus, most lymphoid-resident tumor cells are unlikely to reach the liver for Kupffer cell–mediated depletion, reinforcing the key complementary role of local depletion mechanisms during anti-CD20 therapy.

We next tested the consequence of anti-CD20 treatment in our model. In most preclinical studies, anti-CD20 mAb is administrated very early after tumor inoculation. However, the type and efficiency of depletion mechanisms likely vary once the tumor is fully established, a scenario closer to clinical practice. We therefore compared both early and late anti-CD20 treatment in our model (Fig. 1D). While early treatment cured most animals, late treatment only delayed tumor progression, highlighting limitations in the therapy (Fig. 1E).

A genetically encoded reporter to visualize tumor elimination through apoptosis or phagocytosis

To follow tumor cell fate during anti-CD20 therapy in vivo, we thought to combine intravital imaging with a genetically encoded fluorescent probe. Distinct mechanisms can lead to tumor elimination: In particular, ADCC results in caspase 3–dependent target cell apoptosis, while ADP relies on cell engulfment and degradation (*1*). To visualize cell degradation during ADP, we thought to take advantage of the differential pH sensitivity of cyan fluorescent protein (CFP) and yellow fluorescent protein (YFP) to detect tumor cells residing in acidic phagosomes after engulfment. On the basis of previously described properties of the CFP and YFP (*49*), we expected that YFP fluorescence, but not CFP fluorescence, will be decreasing following phagocytosis (Fig. 2A). We chose to rely on a fluorescence resonance energy transfer (FRET)–based CFP$^{(\mathrm{DEVD})}$YFP reporter, which, beside being a tandem CFP-YFP probe, can also be used to monitor caspase 3 activity reflected by DEVD peptide cleavage (Fig. 2A).

To validate the use of the tandem CFP-YFP probe to monitor ADP, we cultured BM-derived macrophages with CFP$^{(\mathrm{DEVD})}$YFP-expressing lymphoma B cells and followed their fate upon addition of anti-CD20 mAb. As shown in Fig. 2 (B and C), anti-CD20 mAb promoted rapid and efficient phagocytosis of tumor cells. Phagocytosed tumor cells exhibited a progressive loss of YFP, but not CFP, signals as detected by live microscopy and flow cytometry (Fig. 2, C and D, and movie S3). This was not the case for tumor cells before phagocytosis. Loss of YFP was also observed with a version of the tandem fluorescent reporter carrying the linker DEVG insensitive to caspase 3 activity, indicating that these events were not related to apoptosis (fig. S3). To firmly establish that loss of YFP fluorescence was due to the acidic phagosome environment, we repeated this experiment in the presence of the Vacuolar-type ATPase (V-ATPase) inhibitor bafilomycin A1 to block phagosome acidification. In this condition, anti-CD20 treatment was equally effective in triggering tumor engulfment, but YFP fluorescence remained largely unaffected (Fig. 2, E to G). Thus, by acting as a pH sensor, the CFP$^{(\mathrm{DEVD})}$YFP reporter provides direct evidence for tumor cell phagocytosis and subsequent degradation.

Notably, FRET loss with the CFP$^{(\mathrm{DEVD})}$YFP reporter can also reflect apoptosis through caspase 3 activation and cleavage of the DEVD motif. As shown in Fig. 2 (H and I), tumor B cell apoptosis induced by staurosporine also resulted in FRET loss, but by contrast to what was observed during phagocytosis, YFP signals could still be detected upon direct YFP excitation. This was expected as the YFP molecule is cleaved from CFP by caspase 3 but remains intact.

Together, our results establish that the CFP$^{(\mathrm{DEVD})}$YFP reporter can be used both as a pH sensor during phagocytosis and as a reporter for caspase 3 activity during apoptosis. In addition, these two modes of cell death should be easily discriminated from one another. FRET loss during phagocytosis is a slow process following macrophage engulfment, whereas FRET loss by caspase 3 activation is more rapid (*50*, *51*) and should happen before macrophage clearance of the apoptotic body. In the context of anti-CD20 therapy, this reporter should help delineate both ADP and ADCC events in real time.

In vivo imaging reveals the dominant role of phagocytosis in the BM during anti-CD20 therapy

To measure the local antitumor activity mediated by anti-CD20 mAb in the BM, we therefore relied on intravital imaging of tumor cells expressing the CFP$^{(\mathrm{DEVD})}$YFP reporter. We found that anti-CD20 treatment gradually increased the frequency of FRET$^{\mathrm{neg}}$ tumor cells in the imaging field (Fig. 3, A and B, and movie S4). Typically, 10 to 15% of tumor cells exhibited FRET loss after 2 hours of treatment, indicative of antitumor activity (Fig. 3B). No increase in FRET$^{\mathrm{neg}}$ cells was detected in time-lapse movies performed before anti-CD20 mAb injection (Fig. 3, A and B, and movie S4) or after injection of an isotype control (Fig. 3C). To clarify the mode of tumor cell death, we labeled macrophages in vivo using an anti-F4/80 Ab. With this strategy, we could visualize tumor phagocytosis events in the BM immediately after anti-CD20 mAb administration (Fig. 4, A and B, and movies S5 to S7). In some instances, a single macrophage could engulf multiple tumor cells as previously observed in vitro (fig. S4 and movie S8) (*52*). We also recorded FRET loss in a subset of phagocytosed tumor cells (Fig. 4A and movies S5 to S8). Notably, not all phagocytosed tumors showed FRET loss at the end of the in vivo imaging session, most likely because this process required more than 60 min to be detected (Fig. 2C and movie S3). Only very few phagocytosis events were observed in the absence of anti-CD20 Ab (Fig. 4B).

We next thought to more precisely evaluate the contribution of tumor cell death by phagocytosis versus apoptosis. We envisioned

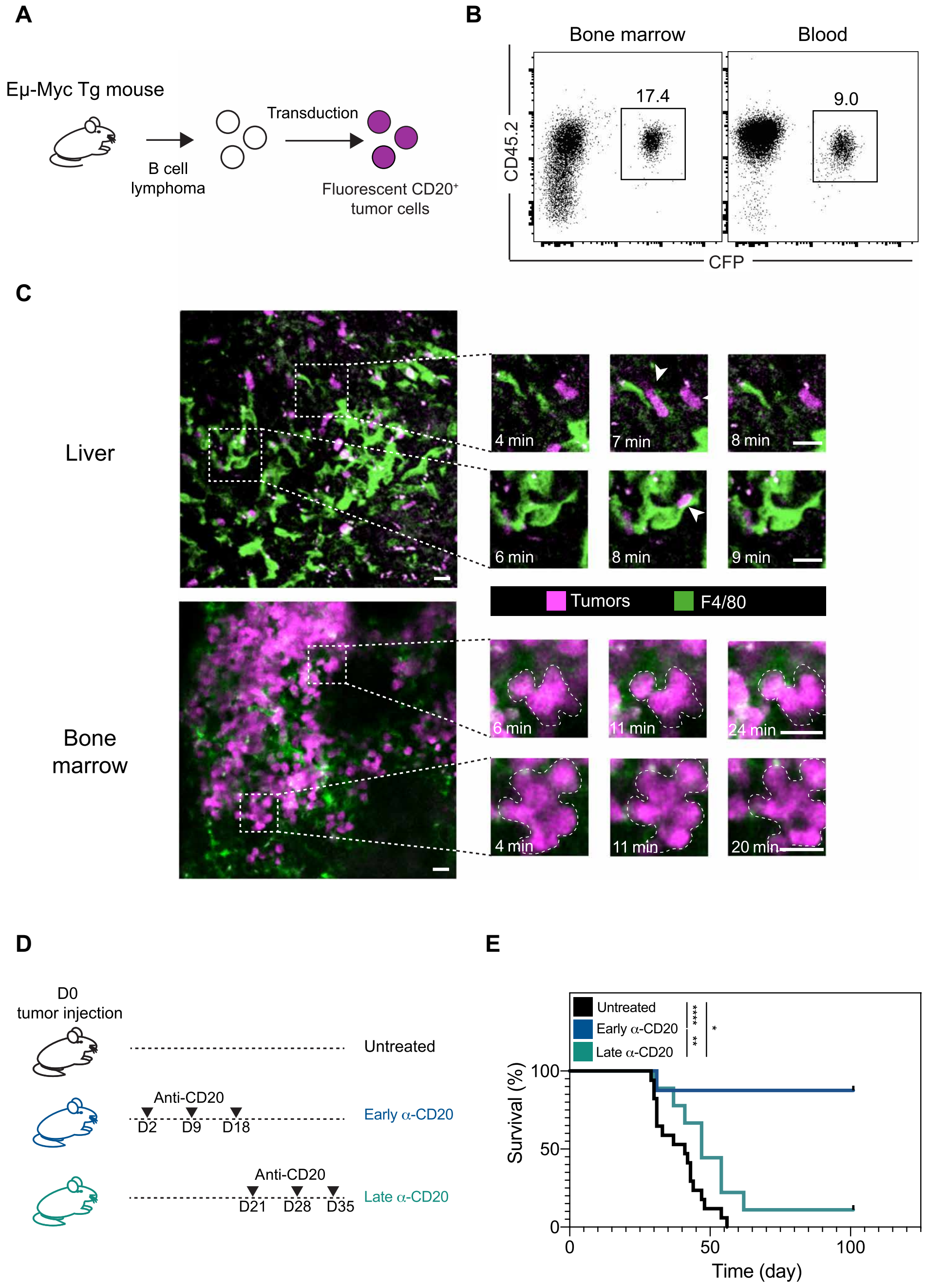

Fig. 1. Distinct motility patterns of lymphoma B cells in different anatomical sites. (**A**) Experimental setup. Eμ-Myc lymphomas were established by intravenous injection of 1×10^6 fluorescent-CD20$^+$ tumor cells in C57BL/6 mice. Recipient mice were analyzed 3 to 4 weeks later. Fluorescent CD20-expressing tumor cells were generated by retroviral transduction of B lymphoma cells isolated from Eμ-myc transgenic mice. (**B**) Representative fluorescence-activated cell sorting (FACS) plots showing cells from the BM and the blood of a tumor-bearing mouse identified as CFP$^+$CD45.2$^+$ cells. Data are representative of four independent experiments with $n = 12$ mice analyzed. (**C**) Representative two-photon time-lapse images of the liver and the BM of tumor-bearing mice in the absence of treatment. Images illustrate that circulating tumors (white arrowheads) are detected in the liver sinusoids but that tumor cells stably reside in the BM. Tumor cells appear in magenta, and F4/80$^+$ macrophages appear in green. Scale bars, 20 μm. Representative of three and five independent experiments for liver and BM imaging, respectively. (**D** and **E**) Different outcomes for tumor-bearing mice treated early or late with anti-CD20 mAb. (D) Schematic of the survival study and the kinetics of treatments. (E) Survival curve for mice treated early or late with anti-CD20 Ab or left untreated. Results are compiled from two independent experiments with 8 to 17 mice per group. Log-rank test was used for statistical analysis. ***$P < 0.001$; **$P < 0.01$; *$P < 0.05$.

at least two outcomes (Fig. 4C). Tumor cells eliminated by phagocytosis should be typically engulfed while being FRET^{pos} and would lose FRET signals only at relatively late time points while being located within macrophages. By contrast, tumor cells undergoing apoptosis (e.g., triggered by NK cell–mediated ADCC) should lose FRET signals first and then possibly be cleared by local macrophages. Of note, while ADCC may not be as effective in mice as in humans (*53*, *54*), mouse NK cells were capable of lysing tumor cells in vitro

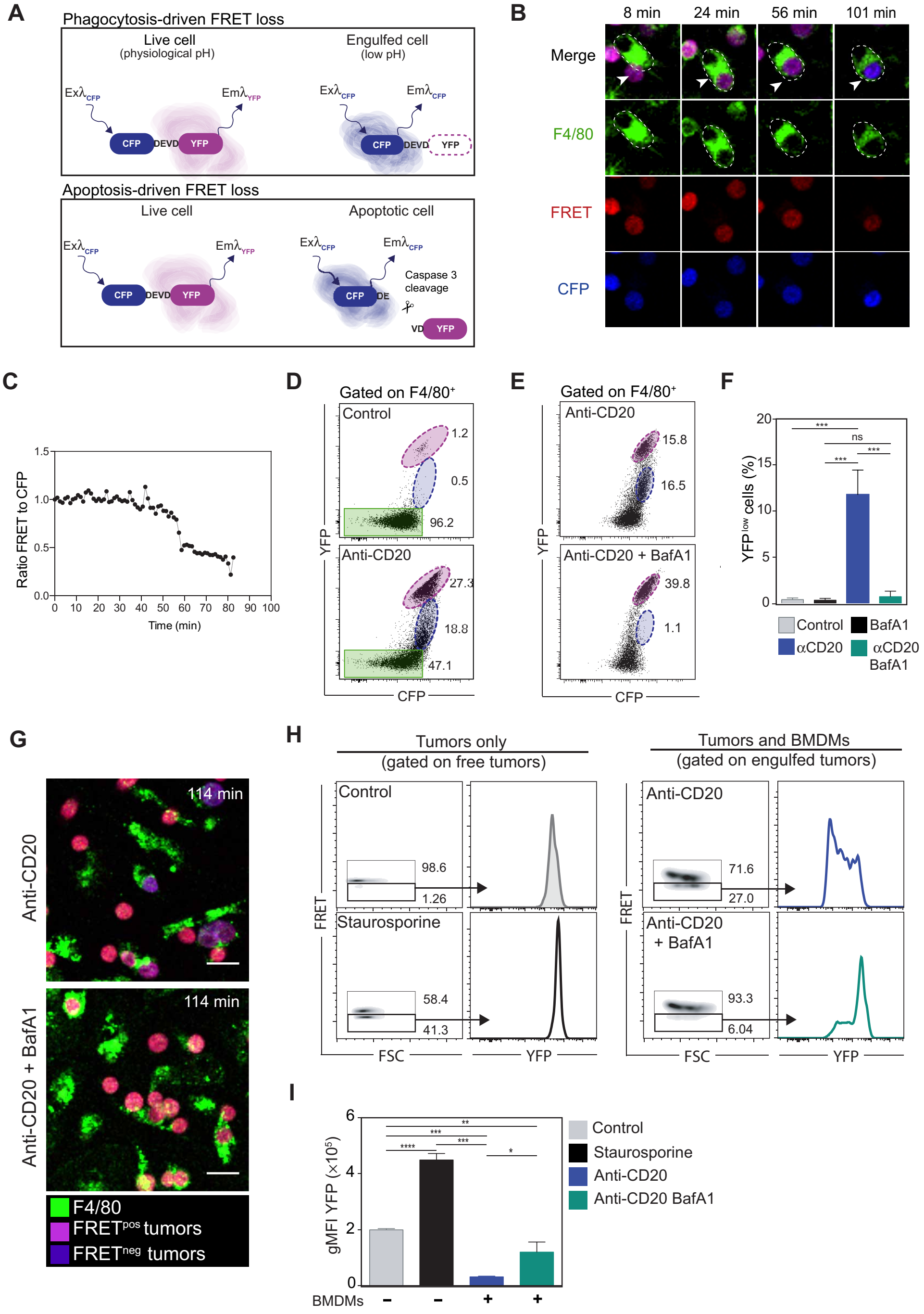

Fig. 2. Real-time visualization of tumor elimination through apoptosis or phagocytosis. (**A**) Principle of the $\text{CFP}^{(\text{DEVD})}$YFP reporter. During phagocytosis, the acidic environment causes a loss of YFP signals in tumor cells resulting in FRET loss. FRET loss during apoptosis is due to caspase 3–dependent cleavage of the $\text{CFP}^{(\text{DEVD})}$YFP reporter (preserving YFP fluorescence). Ex, excitation; Em, emission. (**B** to **G**) Phagocytosis of tumor cells cocultured with macrophages. (B) Time-lapse images following anti-CD20 mAb treatment in vitro. Upon FRET loss, tumor cells switch from magenta to blue. (C) Ratio of FRET to CFP signals for the engulfed tumor cell in (B). Representative of four experiments. (D) Detection of tumor cell phagocytosis by flow cytometry. Macrophage-associated cells with high (magenta) and low (blue) levels of YFP are detected in the presence of anti-CD20 Ab. Macrophages without tumors are highlighted in green. Representative of five experiments. (E and F) Loss of YFP fluorescence during phagocytosis depends on phagosome acidification. (E) FACS plots and bar graphs (F) showing the lack of YFP^{low} cells within macrophages treated with bafilomycin A1. ***$P < 0.001$; ns, nonsignificant. (G) Images showing the lack of FRET loss in tumor cells engulfed by macrophages treated with bafilomycin A1. Scale bars, 20 μm. (**H**) FRET and YFP signals in cells dying by apoptosis (left; staurosporine treatment) or eliminated by phagocytosis (right; engulfed tumors). BMDM, bone marrow–derived macrophage; FSC, forward scatter. (**I**) YFP geometric mean fluorescence intensity for the indicated conditions. Representative of three experiments. ***$P < 0.001$; **$P < 0.01$; *$P < 0.05$.

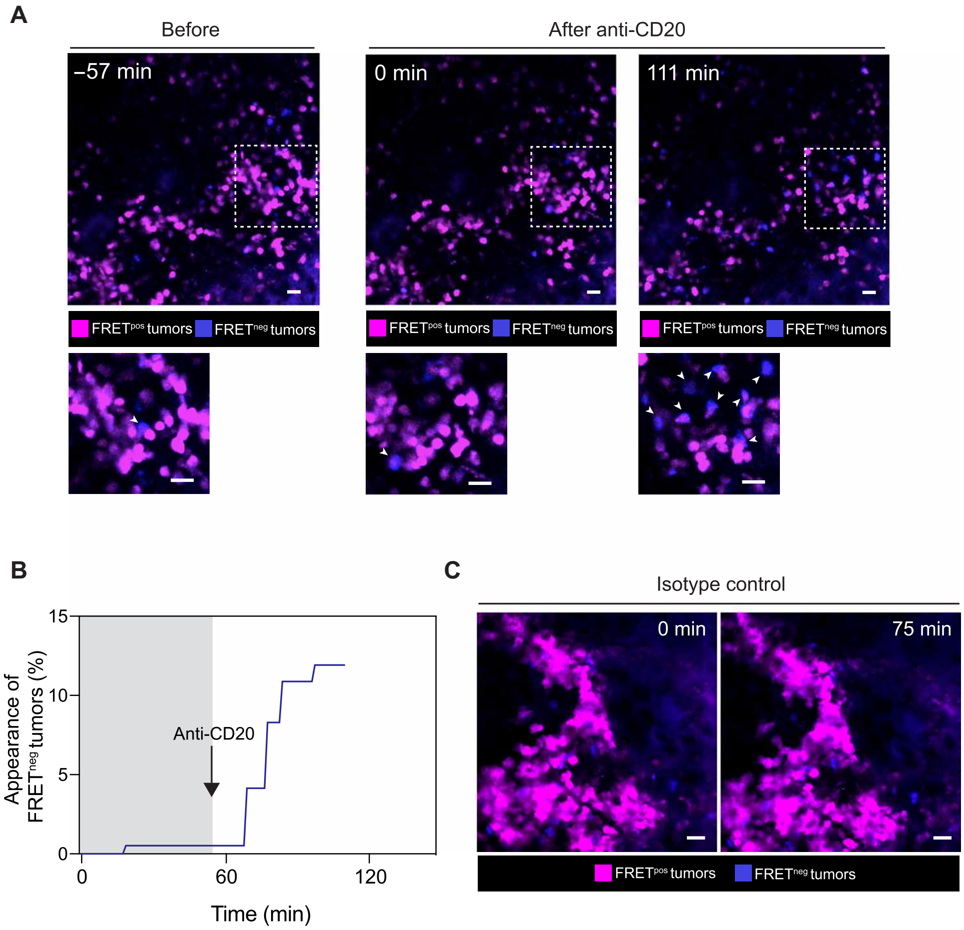

Fig. 3. Real-time detection of tumor cell death events in vivo following anti-CD20 Ab injection. C57BL/6 mice were injected intravenously with 1 × 10^6 tumor cells and were subjected to BM intravital imaging 3 to 4 weeks later before and after anti-CD20 mAb administration. (**A**) Representative two-photon time-lapse images showing the appearance of FRET^{neg} tumor cells (white arrowheads) following anti-CD20 mAb injection. Scale bars, 20 μm. (**B**) Kinetics of appearance of FRET^{neg} tumors before and after anti-CD20 mAb administration as detected by intravital imaging (as a percentage of total tumor cells). Data from three movies were compiled for quantification. (**C**) Representative two-photon time-lapse images showing that virtually all tumors remain FRET^{pos} in the presence of an isotype control. FRET^{pos} tumors are shown in magenta, and FRET^{neg} tumors are shown in blue. Scale bars, 20 μm. Data are representative of $n > 10$ movies and from at least four independent mice.

in the presence of mouse anti-CD20 Ab (fig. S5). While we found in vivo evidence for both outcomes (Fig. 4D and movie S9), the vast majority (>90%) of tumor cell elimination could be attributed to ADP, independently of previous apoptosis (Fig. 4E). To confirm the predominant role of ADP in mediating anti-CD20 antitumor activity, we depleted macrophages using chlodronate liposomes. We observed efficient depletion of BM-associated macrophages ($\text{F4/80}^{\text{high}}$). In these settings, minimal tumor FRET loss was visualized by BM intravital imaging after anti-CD20 injection (fig. S6) compared to nondepleted mice (Fig. 3B). This result further confirms the importance of ADP by BM-associated macrophages for mediating anti-CD20 mAb. ADP was not restricted to our mouse anti-CD20 mAb, as we also observed phagocytosis of human CD20-expressing B cell tumors in the BM of human CD20 transgenic mice injected with rituximab (fig. S7). We have previously shown that depletion of circulating B cell targets is completed within 2 hours (*17*, *18*). To test whether a similar efficiency is measured in the BM, we examined the fate of tumor cells several hours after anti-CD20 Ab injection. Notably, the vast majority of tumor cells were not eliminated at this stage, suggesting some limitations associated with the therapy (Fig. 4F and fig. S8). Together, these results show that ADP is the main mechanism of action driving tumor cell elimination after anti-CD20 therapy yet may not be sufficient for full tumor eradication.

Spatiotemporal limitations during anti-CD20 therapy in vivo

The partial depletion of tumor cells in the BM was consistent with the moderate improvement in survival seen with late administration of anti-CD20 Ab (Fig. 1A). To identify potential bottlenecks in anti-CD20 Ab therapy, we first examined the kinetics of ADP following treatment. Compiling 67 phagocytosis events, we observed that tumor engulfment was initiated as early as a few minutes after Ab injection (Fig. 5A). ADP followed a wave-like pattern occurring within a short time frame. ADP events became rare after 1 hour despite the persistence of macrophages and tumor targets (Fig. 5B). As shown in Fig. 5C, cell degradation (as detected by FRET loss) after phagocytosis often required at least an hour in vivo. After the initial burst of antitumor activity, minimal cell death (either by apoptosis or phagocytosis) was detected for at least 4 hours (fig. S9). To test whether the poor macrophage activity after the initial burst could be due to a lack of available mAb, we measured circulating

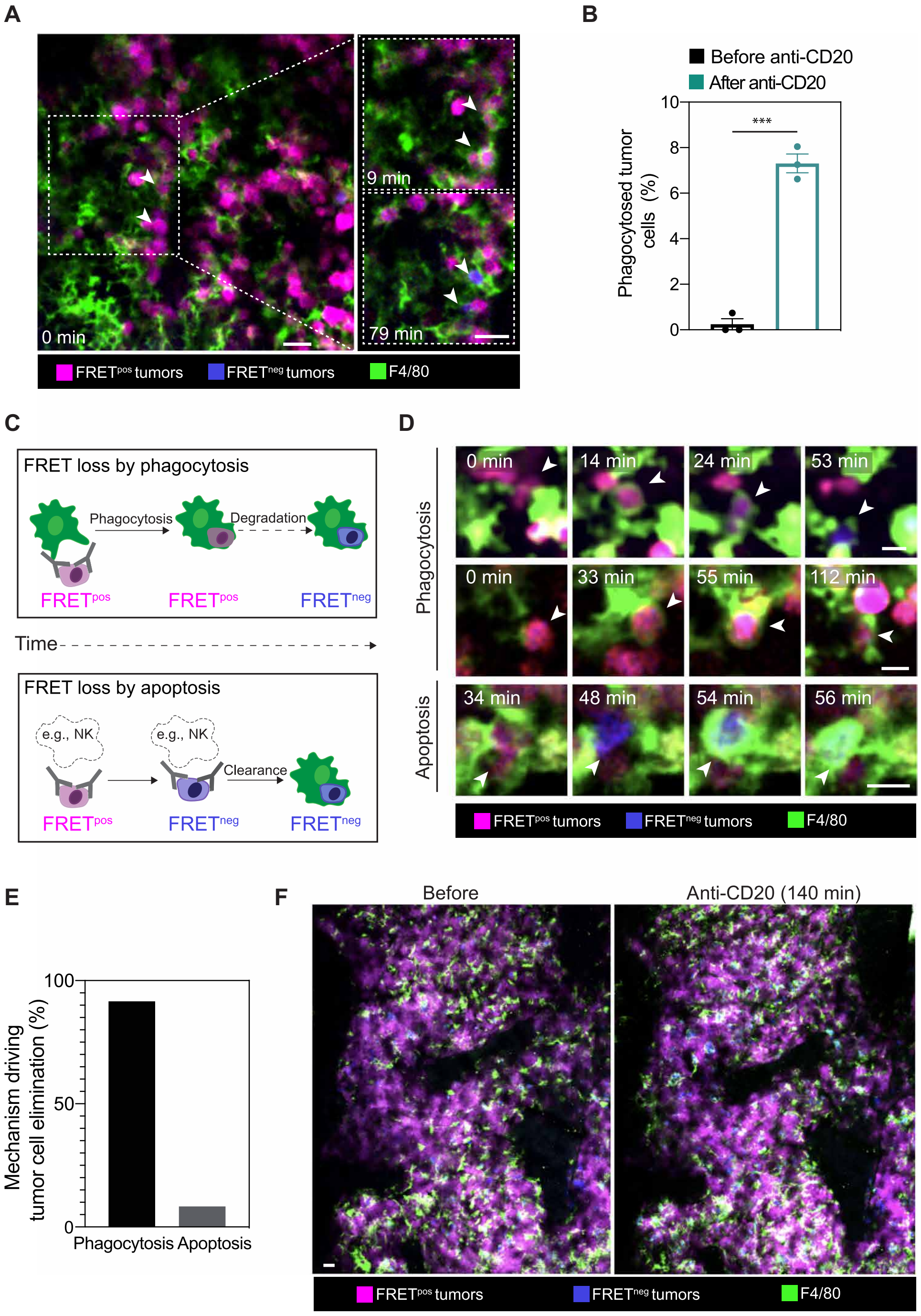

Fig. 4. ADP is the major mechanism of tumor depletion in the BM in response to anti-CD20 mAb. (**A**) Two-photon images from the BM showing phagocytosis events (white arrowheads) resulting in FRET loss in engulfed tumors. FRET^{pos} tumors are shown in magenta, FRET^{neg} tumors are shown in blue, and macrophages are shown in green. Scale bars, 20 μm. (**B**) Phagocytosis of FRET^{pos} tumor cells is triggered by anti-CD20 mAb. Phagocytosis events were quantified during 1 hour either before or immediately after anti-CD20 Ab. Compiled from three independent movies in a representative mouse out of four. $^{***}P < 0.001$ (unpaired Student's *t* test). (**C**) Schematic illustrating FRET loss in tumor cells dying after phagocytosis or apoptosis following anti-CD20 therapy. During ADP, FRET loss happens after engulfment. During apoptosis (e.g. ADCC by NK cells), tumors first lose FRET signals before being cleared by macrophages. (**D**) Time-lapse images of putative ADP or apoptotic events. Scale bars, 20 μm. (**E**) ADP is the primary mechanism of tumor depletion in the BM following anti-CD20 therapy. Contribution of cell death mechanisms during anti-CD20 therapy. Each tumor cell death ($n = 67$) was classified as an ADP or apoptotic event as detailed in (C). (**F**) Anti-CD20 therapy shows limited efficacy in the BM. Imaging was performed 140 min after anti-CD20 mAb. Scale bar, 20 μm. Representative of $n > 10$ movies from at least four independent mice.

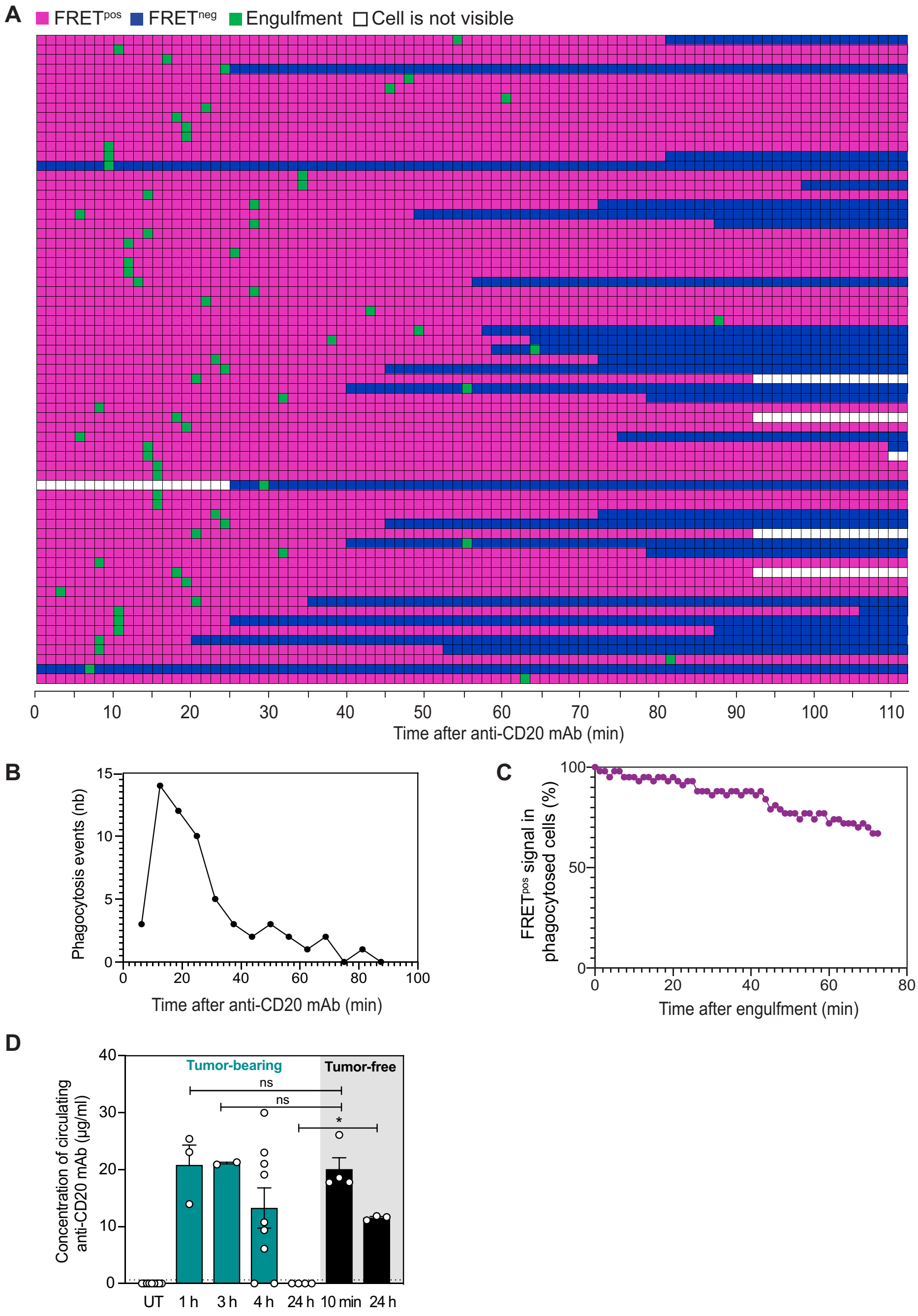

Fig. 5. Kinetics of ADP events during anti-CD20 therapy. C57BL/6 mice were injected intravenously with 1 × 10^6 tumor cells and were subjected to BM intravital imaging 3 to 4 weeks later just before and after anti-CD20 mAb administration. (**A**) Kinetics of FRET loss and phagocytosis in tumor cells. Each horizontal line represents a tumor cell eliminated during the imaging period (as detected by FRET loss). Colored squares show the time points during which the tumor is visible within the imaging field. Magenta and blue indicate the time period during which the tumor cell is FRET^{pos} and FRET^{neg}, respectively. Green squares indicate the time point at which tumor cells are engulfed by macrophages. (**B**) Kinetics of ADP events after anti-CD20 treatment. nb, number. (**C**) The timing of FRET loss was quantified for each tumor cell from the time of phagocytosis. Data from (A) to (C) were compiled from $n > 10$ movies obtained from at least four independent tumor-bearing mice. (**D**) Concentration of circulating anti-CD20 mAb in tumor-bearing mice that were left untreated (UT) or treated for the indicated time with anti-CD20 mAb (clone 5D2). Concentration of circulating Ab was also quantified in tumor-free mice treated for 10 min or 24 hours. A Mann-Whitney statistical test was performed for statistical significance. $^*P < 0.05$.

mAb levels in tumor-bearing mice at different time points after mAb injection. As shown in Fig. 5D, anti-CD20 could still be detected at high concentration up to 4 hours after injection. These results suggest that a phase of macrophage hyporesponsiveness rather than mAb availability contributes to the wave-like dynamics of ADP.

Notably, anti-CD20 mAb concentration sharply decreased at 24 hours in tumor-bearing mice while remaining abundant in tumor-free animals (Fig. 5D). Thus, mAb consumption/sequestration by tumor targets seen at later stage (24 hours) may further impair mAb treatment efficacy. Consistently, we did not detect substantial tumor cell death events when in vivo imaging was performed at 24 hours after treatment (fig. S10). Overall, the transient phase of ADP in vivo reveals a strong temporal limitation of the therapy.

Given the dominance of ADP during response to anti-CD20 mAb, we asked whether the distribution of macrophages within the tumor

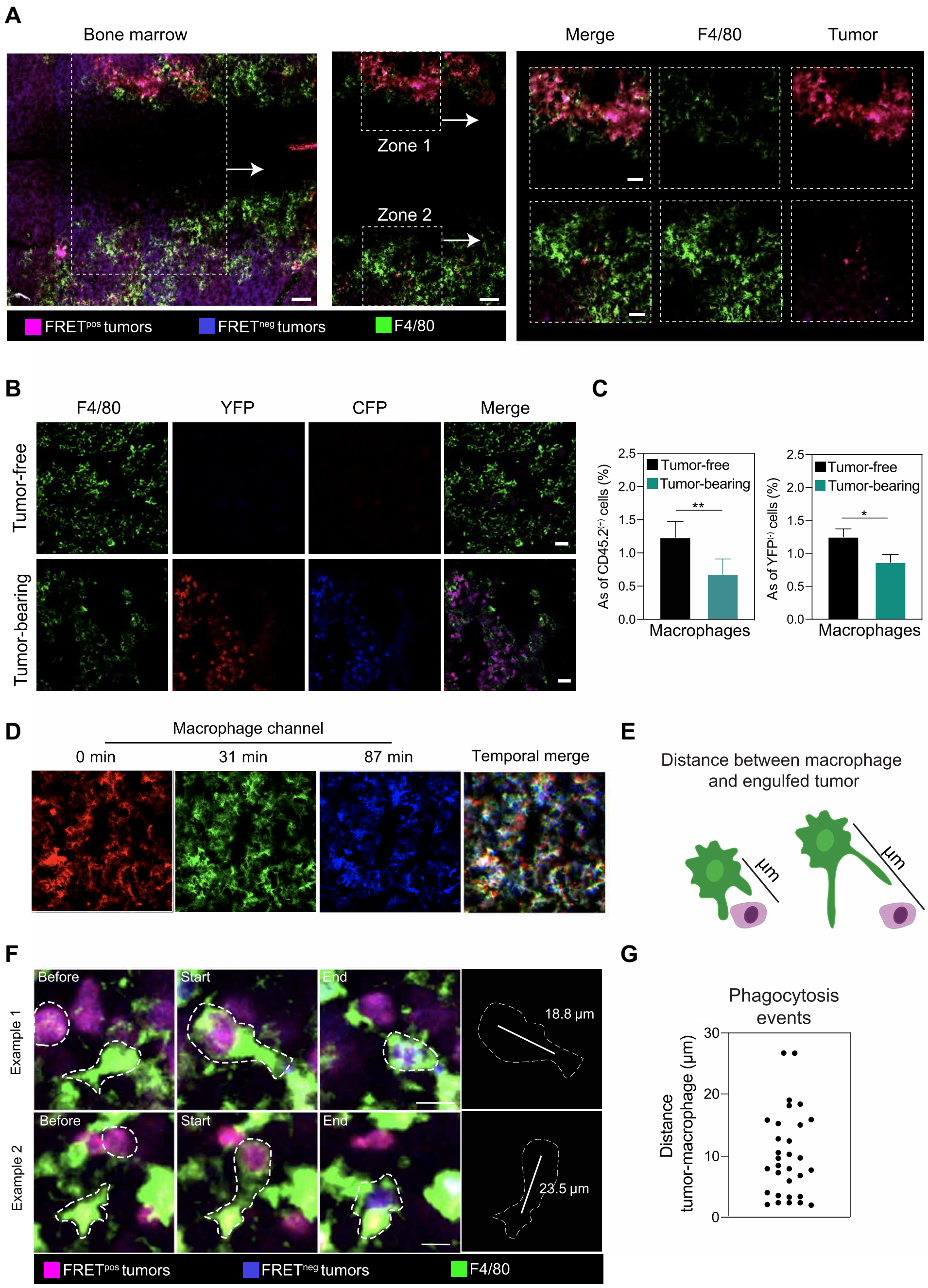

Fig. 6. The density of macrophages is a limiting factor during anti-CD20 therapy in vivo. (**A**) Representative two-photon image of the BM comparing macrophage density in tumor-rich area (zone 1) and a tumor-free zone (zone 2) within the same imaging field. Scale bars, 100 μm; inset scale bars, 50 μm. (**B**) The density of BM-associated macrophages in tumor-bearing or tumor-free mouse is shown by immunofluorescence on frozen BM sections. (**C**) Bar graph showing the percentage of macrophages (CD11b$^+$Ly6G$^-$Ly6C^{low}F4/80$^+$ cells) in the BM within total CD45.2$^+$ cells or within YFP$^-$ cells (excluding tumor cells), as determined by flow cytometry. Representative of two independent experiments. A Mann-Whitney statistical test was performed for statistical significance. **$P < 0.01$; *$P < 0.05$. (**D**) BM-associated macrophages are mostly sessile. Representative time-lapse images of F4/80$^+$ macrophages in the BM. A color was attributed to each time point and overlaid to visualize the migratory phenotype of macrophages. Superimposed signals appear in white and reflect the lack of macrophage motility. (**E** and **F**) Quantification of the distance of macrophage survey. (E) Schematic illustrating the distance separating the targeted tumor cell from the macrophage center and (F) representative images from intravital imaging of the BM. (**G**) Compilation of distances recorded for individual ADP events.

may also represent a limiting factor for the efficacy of the therapy. Notably, there was a sharp decrease in the density of BM-associated macrophages in tumor-bearing mice compared to control animals (Fig. 6, A to C). Specifically, macrophages appeared to be less dense in tumor-rich patches, suggesting spatial exclusion (Fig. 6A). To rule out the possibility that poor macrophage staining in vivo was due to limited F4/80 Ab diffusion within dense tumor structures, we performed immunofluorescence on fixed BM tissue sections. As shown in Fig. 6B, we confirmed that tumor-rich region exhibited a lower macrophage density as compared to noninfiltrated areas of the BM or to tumor-free control animals. One possibility could be that tumor B cells preferentially seed macrophage-sparse areas, but we do not favor this hypothesis as individual tumor cells were found in macrophage-rich regions in mice with low tumor burden (fig. S11). Moreover, flow cytometric analysis also confirmed that tumor-bearing mice exhibited a decreased percentage of macrophages in the BM (Fig. 6C). The decreased presence of macrophages likely represents an additional limitation given that BM-associated macrophages appeared largely sessile (Fig. 6D and movie S10). To support this idea, we measured for phagocytic events the distance initially separating the targeted tumor cell from the macrophage center (Fig. 6, E and F). We found that macrophages could, at best, reach tumor cells located 30 μm away (Fig. 6G). Overall, our results suggest that macrophage sparseness and low motility, together with the sessile behavior of tumor cells, may strongly limit the number of tumor cells reachable for ADP. Together, our in vivo dynamic analyses uncovered both spatial and temporal bottlenecks in ADP of non-circulating malignant B cells in response to anti-CD20 therapy.

DISCUSSION

In the present report, we have established an in vivo imaging approach aimed at providing a detailed mechanistic understanding of the antitumor activity mediated by anti-CD20 mAb. In a model of MYC-driven B cell lymphoma developing primarily in the BM, we established that ADP, but not ADCC, was the major mode of tumor elimination. Antitumor activity started rapidly after mAb administration but was terminated within 1 to 2 hours. Moreover, ADP was also limited by the lack of motility of both tumor cells and macrophages. Moreover, this limitation was exacerbated in tumor-rich areas where macrophages were present at low density. Our results support the idea that the rate of ADP is a limiting factor during anti-CD20 therapy.

Several approaches are available to interrogate the mode of action of tumor-targeting mAb therapy. These include in vitro experiments with human cells as well as preclinical models relying on cell depletion or genetic ablation of specific receptors (e.g., Fc receptors) (*14*–*22*). Intravital imaging provides key additional insights by offering direct visualization of cellular mechanisms and quantitative measurements of cell processes while addressing spatiotemporal variability in therapeutic efficacy (*55*). Moreover, the use of functional reporter in imaging experiment can further refine these analyses (*56*). While several studies have identified macrophages with engulfed tumors on fixed tissue sections (*20*, *22*, *39*), it is difficult to formally exclude that tumors were not initially killed by a distinct effector and subsequently cleared by macrophages. Here, we described a fluorescent genetically encoded reporter to help delineate cell death mechanisms in real time during mAb therapy. With this probe, we found little evidence of cell death by apoptosis upon anti-CD20 treatment but revealed instead a dominant role for phagocytosis and subsequent cell degradation in tumor elimination. Of the tumors that were eliminated, more than 90% were targeted by ADP. Thus, our dynamic analyses extend previous studies by providing direct evidence and quantitative measurements for the role of ADP by BM-associated macrophages.

Previous studies have highlighted that anti-CD20 mAb activity can be suboptimal, in particular in the BM (*25*, *38*, *39*). This activity could be enhanced through chemotherapy (*39*) or by interfering with "don't eat me" signals (*26*, *44*–*46*). To more precisely identify the origins of these limitations, we established the rate and spatial distribution of ADP events. First, we found that ADP events occurred as a rapid but short wave being terminated 1 to 2 hours after mAb administration despite the presence of large amounts of circulating anti-CD20 mAb at these time points. These observations may constitute in vivo evidence for saturation of phagocytosis at the tumor site, a phenomenon previously described for human macrophages in vitro (*52*) or Kupffer cells (*57*) in vivo, in which the phagocytic capacity is lost after an initial round of target engulfment. Thus, strategies aimed at understanding and bypassing this early phase of hyporesponsiveness in ADP may sustain and potentiate anti-CD20 mAb activity. Beyond this phase of hyporesponsiveness, the phagocytic capacity of macrophages may be further limited at later time points due to Ab consumption/sequestration observed here and elsewhere at high tumor burden (*58*).

Second, we found that macrophages were largely sessile, thus surveying a relatively limited territory for phagocytosis. Macrophages could target, at best, tumor cells located at 30 μm from their center. Furthermore, macrophages were found to be less numerous in the BM of tumor-bearing mice and particularly were excluded from tumor-rich regions. These findings likely provide a basis for the observed positive correlation between anti-CD20 clinical response and macrophage density in patients with follicular lymphoma (*59*). Strategies to boost the accumulation of phagocytic cells at the tumor site may therefore represent an interesting avenue for improved Ab-mediated cellular toxicity.

In sum, by using functional in vivo imaging, we have highlighted the rapid and dominant role of ADP in the BM during anti-CD20 Ab therapy in a model of MYC-driven B cell lymphoma. Furthermore, by uncovering the spatiotemporal dynamics of anti-CD20 antitumor activity, we revealed important bottlenecks that should be considered to potentiate treatment efficacy. The ability to measure mAb functional activity at the single-cell level should offer new opportunities to guide the development of novel therapeutic strategies or combination therapies.

MATERIALS AND METHODS

Mice and cell lines

Six- to 8-week-old C57BL/6J mice were purchased from ENVIGO. Eμ-myc transgenic mice developing a spontaneous Burkitt-like lymphoma (*47*) were bred in our animal facility. A Burkitt-like lymphoma B cell line was isolated from male Eμ-myc mice and transduced to express a FRET-based reporter [CFP$^{(DEVD)}$YFP probe (Eμ-myc DEVD cells) or CFP$^{(DEVG)}$YFP probe (Eμ-myc DEVG cells)] and express CD20. These cells were then established in C57BL/6 mice by injecting 1×10^6 Eμ-myc cells intravenously. Mice were examined every day and sacrificed in case of prostration, tousled hair, weakness, ectopic or nodal tumor mass >1 cm, or a weight loss >10%.

All animal studies were approved by the Pasteur Institute Safety Committee in accordance with French and European guidelines (CETEA 2017-0038). Cells were cultured in RPMI supplemented with 10% heat-inactivated fetal bovine serum, penicillin (50 U ml^{-1}), streptomycin (50 μg ml^{-1}), 1 mM sodium pyruvate, 10 mM Hepes, and 50 μM 2-mercaptoethanol and maintained at 37°C and 5% CO_2. Cell lines were routinely tested for the absence of mycoplasma contamination (Venor-GeM Advance Mycoplasma Detection Kit, Minerva Biolabs).

Treatments

Anti-CD20 mAb (clone 5D2, mouse IgG2a, from Genentech) was used at 20 μg ml^{-1} in vitro. Mice were injected intravenously with 50 μg of 5D2 or 50 μg of the isotype control HY1.2 (mIgG2a) when indicated. In some experiments, cells were pretreated for 1 hour with bafilomycin A1 (Fisher Scientific) at 50 mM before anti-CD20 mAb addition, and bafilomycin A1 was left throughout the assay. Tumors were treated overnight with staurosporine (Sigma-Aldrich) at a final concentration of 1 μM to induce apoptosis. Mice received 200 μl of rituximab, an anti-human CD20 IgG1 Ab, when indicated.

Flow cytometry

For flow cytometric analysis, cell suspensions were Fc-blocked using anti-CD16/32 mAb (BioLegend, clone 93) combined to murine serum 4% (Thermo Fisher Scientific). Stainings were performed with the following mAb: CD45.2-BUV737 (clone 104, BD), Ly6G-BUV395 (clone 1A8, BD), Ly6C-BV785 (clone HK1.4, BioLegend), CD11b-PerCp5.5 (clone M1/70, BioLegend), F4/80–Alexa Fluor 594 (BM8, BioLegend), F4/80-APC (allophycocyanin) (BM8, BioLegend), F4/80-APCCy7 (BM8, BioLegend), mCD20–Alexa Fluor 647 (clone SA275A11, BioLegend), and anti-IgG–PE (phycoerythrin) (poly4053, BioLegend). Analyses were performed with an LSRFortessa II cytometer (BD Biosciences) or a CytoFLEX LX (Beckman Coulter) and analyzed with FlowJo software version 10.6.2 (BD Biosciences).

BM extraction, BM-derived macrophage generation, and ADP assay

For ex vivo analyses, femurs and tibias were isolated from Eμ-myc tumor-bearing mice or control C57BL/6 mice. BM cells were extracted by centrifugation of the bones into phosphate-buffered saline (PBS) supplemented with 1 mM EDTA and 0.5% fetal bovine serum [fluorescence-activated cell sorting (FACS) buffer], and single-cell suspensions were prepared by filtering the cells through 70-μm cell strainers for further experiment. To generate BM-derived macrophages, 20 × 10^6 cells were resuspended in RPMI 20% macrophage colony-stimulating factor (M-CSF) (from L929 supernatant) and plated onto a low-adhering 150 mm × 25 mm dish treated by vacuum gas plasma plate (Corning REF353025) for a total of 7 days. At day 4, supernatant was removed and fresh RPMI 20% L929 was added. Macrophages were then detached by PBS–5 mM EDTA for 10 min at 4°C before being plated at 1 × 10^6 cells in 12-well plates and left overnight before doing an ADP assay the following day: 1 × 10^6 tumor cells were added to the well and left 30 min at 37°C to settle down before being treated with the indicated treatment for 2 hours at 37°C. Phagocytosed tumor cells were quantified by flow cytometry.

Intravital two-photon imaging

C57BL/6 mice were injected intravenously with 1 × 10^6 tumor cells and subjected to BM intravital imaging 3 to 4 weeks later before and after anti-CD20 mAb. Macrophages were visualized in vivo by injecting an F4/80 fluorescent mAb. Briefly, mice were anesthetized with a mixture of xylazine (Rompun; 10 mg/kg) and ketamine (Imalgene; 100 mg/kg), which was replenished hourly. The scalp hair was removed, and the skin was incised at the midline to expose the bone. The jaw was fixed on the surface of a steel plate to maintain the superior part of the skull horizontally, and a round 20-mm coverslip was centered and fixed above the frontoparietal suture after PBS deposition using a cyanoacrylate-based glue. During imaging, mice were supplied with oxygen and their temperature was maintained at 37°C with a heating pad. Two-photon imaging was performed with an upright microscope FVMPE-RS (Olympus) and a 25×/1.05 numerical aperture (NA) water-dipping objective (Olympus). Excitation was provided by an InSight DeepSee dual laser (Spectra Physics) tuned at 820 nm. To create time-lapse sequences, we typically scanned a 30- to 50-μm-thick volume of tissue at 5-μm Z-steps and 75-s intervals. The following filters were used for fluorescence detection: CFP (483/32), YFP (542/27), and Alexa Fluor 594 (593/35). Movies were processed and analyzed with Fiji software (ImageJ 2.0). Cell death events (FRET loss) and phagocytosis events were quantified manually and computed to the total number of tumor cells in the imaging field. Movies and figures based on two-photon microscopy are shown as two-dimensional (2D) maximum intensity projections of 3D data.

Fixed tissue section of the BM and confocal microscopy

Tibia were dissected and left for 4 hours in 1% paraformaldehyde and subsequently transferred to 0.35 M EDTA for decalcification. Tissues were dehydrated in 20% sucrose and frozen in OCT embedding compound (Tissue-Tek, Sakura Finetek). Eight-micrometer-thick tissue sections were rehydrated and Fc-blocked with normal mouse and rat serums in the presence of 0.3% Triton X-100 (Sigma-Aldrich). Tissues were stained with F4/80-APC (clone BM8, BioLegend), and tumors were visualized using their CFP or YFP fluorescence. Sections were imaged using a Leica TCS SP5 confocal microscope. Images were processed using Fiji software (ImageJ 2.0).

ADCC assay

Splenocytes from Rag$^{-/-}$ mice were cultured at 0.3 × 10^6 cells/ml in a 96-well plate for 5 days in the presence of recombinant human interleukin-2 (200 U/ml; R&D Systems). NK cells were purified by negative magnetic selection (Miltenyi), and purity was confirmed by flow cytometry. Tumor cells (20 × 10^4) were either left untreated or treated with anti-CD20 Ab (25 μg/ml) (clone 5D2, Genentech) for 30 min before NK cells were added at the indicated Effector:Target (E:T) ratios. The number of tumor cells was determined by flow cytometry and used to calculate the percentage of tumor lysis in the indicated different conditions.

Ab titration in the blood by flow cytometry

To determine Ab concentrations in serum, we adapted the S-Flow technique (*60*). Briefly, human embryonic kidney (HEK) cells were transfected (jetPRIME, Polyplus) to express mouse CD20 or left untreated (control). CD20-expressing HEK cells (4 × 10^4) were plated in a 96-well plate and stained with sera (diluted at 1:200) collected from individual mice for 30 min at 4°C. A secondary PE-conjugated anti-IgG was used to quantify cell-bound anti-CD20 Ab (clone 5D2). A reference curve was obtained by direct incubation of CD20$^+$HEK cells with known concentration of purified anti-CD20 mAb. Mean fluorescence intensity of individual samples (ran in duplicates) was compared to the reference curve to determine circulating Ab concentrations.

Macrophage depletion using chlodronate liposome

To deplete macrophages, tumor-bearing mice were treated intravenously with 200 μl of clodronate liposome (Liposoma) at 48 and 24 hours before two-photon imaging. Efficient depletion in the BM was confirmed by flow cytometry.

Statistical analysis

All statistical tests were performed with Prism v.8 (GraphPad). A log-rank, Mann-Whitney, or one-way analysis of variance (ANOVA) was used as indicated. Data are expressed as mean ± SEM.

SUPPLEMENTARY MATERIALS

Supplementary material for this article is available at http://advances.sciencemag.org/cgi/content/full/7/8/eabd6167/DC1

View/request a protocol for this paper from *Bio-protocol*.

REFERENCES AND NOTES

1. T. M. Pierpont, C. B. Limper, K. L. Richards, Past, present, and future of rituximab—The world's first oncology monoclonal antibody therapy. *Front. Oncol.* **8**, 163 (2018).
2. A. C. Chan, P. J. Carter, Therapeutic antibodies for autoimmunity and inflammation. *Nat. Rev. Immunol.* **10**, 301–316 (2010).
3. M. Biburger, S. Aschermann, I. Schwab, A. Lux, H. Albert, H. Danzer, M. Woigk, D. Dudziak, F. Nimmerjahn, Monocyte subsets responsible for immunoglobulin G-dependent effector functions in vivo. *Immunity* **35**, 932–944 (2011).
4. M. S. Cragg, S. M. Morgan, H. T. C. Chan, B. P. Morgan, A. V. Filatov, P. W. M. Johnson, R. R. French, M. J. Glennie, Complement-mediated lysis by anti-CD20 mAb correlates with segregation into lipid rafts. *Blood* **101**, 1045–1052 (2003).
5. O. Middleton, E. Cosimo, E. Dobbin, A. M. McCaig, C. Clarke, A. M. Brant, M. T. Leach, A. M. Michie, H. Wheadon, Complement deficiencies limit CD20 monoclonal antibody treatment efficacy in CLL. *Leukemia* **29**, 107–114 (2015).
6. N. D. Gaetano, E. Cittera, R. Nota, A. Vecchi, V. Grieco, E. Scanziani, M. Botto, M. Introna, J. Golay, Complement activation determines the therapeutic activity of rituximab in vivo. *J. Immunol.* **171**, 1581–1587 (2003).
7. M. S. Cragg, M. J. Glennie, Antibody specificity controls in vivo effector mechanisms of anti-CD20 reagents. *Blood* **103**, 2738–2743 (2004).
8. L. Rougé, N. Chiang, M. Steffek, C. Kugel, T. I. Croll, C. Tam, A. Estevez, C. P. Arthur, C. M. Koth, C. Ciferri, E. Kraft, J. Payandeh, G. Nakamura, J. T. Koerber, A. Rohou, Structure of CD20 in complex with the therapeutic monoclonal antibody rituximab. *Science* **367**, 1224–1230 (2020).
9. W. Wang, A. K. Erbe, J. A. Hank, Z. S. Morris, P. M. Sondel, NK cell-mediated antibody-dependent cellular cytotoxicity in cancer immunotherapy. *Front. Immunol.* **6**, 368 (2015).
10. L. M. Weiner, R. Surana, S. Wang, Monoclonal antibodies: Versatile platforms for cancer immunotherapy. *Nat. Rev. Immunol.* **10**, 317–327 (2010).
11. P. Boross, J. H. W. Leusen, Mechanisms of action of CD20 antibodies. *Am. J. Cancer Res.* **2**, 676–690 (2012).
12. M. J. Glennie, R. R. French, M. S. Cragg, R. P. Taylor, Mechanisms of killing by anti-CD20 monoclonal antibodies. *Mol. Immunol.* **44**, 3823–3837 (2007).
13. K. R. VanDerMeid, M. R. Elliott, A. M. Baran, P. M. Barr, C. C. Chu, C. S. Zent, Cellular cytotoxicity of next-generation CD20 monoclonal antibodies. *Cancer Immunol. Res.* **6**, 1150–1160 (2018).
14. V. Minard-Colin, Y. Xiu, J. C. Poe, M. Horikawa, C. M. Magro, Y. Hamaguchi, K. M. Haas, T. F. Tedder, Lymphoma depletion during CD20 immunotherapy in mice is mediated by macrophage FcγRI, FcγRIII, and FcγRIV. *Blood* **112**, 1205–1213 (2008).
15. J. Uchida, Y. Hamaguchi, J. A. Oliver, J. V. Ravetch, J. C. Poe, K. M. Haas, T. F. Tedder, The innate mononuclear phagocyte network depletes B lymphocytes through Fc receptor–dependent mechanisms during anti-CD20 antibody immunotherapy. *J. Exp. Med.* **199**, 1659–1669 (2004).
16. R. A. Clynes, T. L. Towers, L. G. Presta, J. V. Ravetch, Inhibitory Fc receptors modulate *in vivo* cytoxicity against tumor targets. *Nat. Med.* **6**, 443–446 (2000).
17. F. Montalvao, Z. Garcia, S. Celli, B. Breart, J. Deguine, N. Van Rooijen, P. Bousso, The mechanism of anti-CD20–mediated B cell depletion revealed by intravital imaging. *J. Clin. Investig.* **123**, 5098–5103 (2013).
18. C. L. Grandjean, F. Montalvao, S. Celli, D. Michonneau, B. Breart, Z. Garcia, M. Perro, O. Freytag, C. A. Gerdes, P. Bousso, Intravital imaging reveals improved Kupffer cell-mediated phagocytosis as a mode of action of glycoengineered anti-CD20 antibodies. *Sci. Rep.* **6**, 34382 (2016).
19. F. Nimmerjahn, S. Gordan, A. Lux, FcγR dependent mechanisms of cytotoxic, agonistic, and neutralizing antibody activities. *Trends Immunol.* **36**, 325–336 (2015).
20. B. Lehmann, M. Biburger, C. Brückner, A. Ipsen-Escobedo, S. Gordan, C. Lehmann, D. Voehringer, T. Winkler, N. Schaft, D. Dudziak, H. Sirbu, G. F. Weber, F. Nimmerjahn, Tumor location determines tissue-specific recruitment of tumor-associated macrophages and antibody-dependent immunotherapy response. *Sc. Immunol.* **2**, eaah6413 (2017).
21. Y. Hamaguchi, Y. Xiu, K. Komura, F. Nimmerjahn, T. F. Tedder, Antibody isotype-specific engagement of Fcγ receptors regulates B lymphocyte depletion during CD20 immunotherapy. *J. Exp. Med.* **203**, 743–753 (2006).
22. Q. Gong, Q. Ou, S. Ye, W. P. Lee, J. Cornelius, L. Diehl, W. Y. Lin, Z. Hu, Y. Lu, Y. Chen, Y. Wu, Y. G. Meng, P. Gribling, Z. Lin, K. Nguyen, T. Tran, Y. Zhang, H. Rosen, F. Martin, A. C. Chan, Importance of cellular microenvironment and circulatory dynamics in B cell immunotherapy. *J. Immunol.* **174**, 817–826 (2005).
23. S. de Haij, J. H. M. Jansen, P. Boross, F. J. Beurskens, J. E. Bakema, D. L. Bos, A. Martens, J. S. Verbeek, P. W. H. I. Parren, J. G. J. van de Winkel, J. H. W. Leusen, *In vivo* cytotoxicity of type I CD20 antibodies critically depends on Fc receptor ITAM signaling. *Cancer Res.* **70**, 3209–3217 (2010).
24. N. Gül, L. Babes, K. Siegmund, R. Korthouwer, M. Bögels, R. Braster, G. Vidarsson, T. L. M. ten Hagen, P. Kubes, M. van Egmond, Macrophages eliminate circulating tumor cells after monoclonal antibody therapy. *J. Clin. Invest.* **124**, 812–823 (2014).
25. S. Gordan, H. Albert, H. Danzer, A. Lux, M. Biburger, F. Nimmerjahn, The immunological organ environment dictates the molecular and cellular pathways of cytotoxic antibody activity. *Cell Rep.* **29**, 3033–3046.e4 (2019).
26. M. E. W. Logtenberg, J. H. M. Jansen, M. Raaben, M. Toebes, K. Franke, A. M. Brandsma, H. L. Matlung, A. Fauster, R. Gomez-Eerland, N. A. M. Bakker, S. van der Schot, K. A. Marijt, M. Verdoes, J. B. A. G. Haanen, J. H. van den Berg, J. Neefjes, T. K. van den Berg, T. R. Brummelkamp, J. H. W. Leusen, F. A. Scheeren, T. N. Schumacher, Glutaminyl cyclase is an enzymatic modifier of the CD47- SIRPα axis and a target for cancer immunotherapy. *Nat. Med.* **25**, 612–619 (2019).
27. H. L. Matlung, L. Babes, X. W. Zhao, M. van Houdt, L. W. Treffers, D. J. van Rees, K. Franke, K. Schornagel, P. Verkuijlen, H. Janssen, P. Halonen, C. Lieftink, R. L. Beijersbergen, J. H. W. Leusen, J. J. Boelens, I. Kuhnle, J. van der Werff Ten Bosch, K. Seeger, S. Rutella, D. Pagliara, T. Matozaki, E. Suzuki, C. W. M.-v. der Houven van Oordt, R. van Bruggen, D. Roos, R. A. W. van Lier, T. W. Kuijpers, P. Kubes, T. K. van den Berg, Neutrophils kill antibody-opsonized cancer cells by trogoptosis. *Cell Rep.* **23**, 3946–3959 (2018).
28. M. Albanesi, D. A. Mancardi, F. Jönsson, B. Iannascoli, L. Fiette, J. P. Di Santo, C. A. Lowell, P. Bruhns, Neutrophils mediate antibody-induced antitumor effects in mice. *Blood* **122**, 3160–3164 (2013).
29. G. Cartron, L. Dacheux, G. Salles, P. Solal-Celigny, P. Bardos, P. Colombat, H. Watier, Therapeutic activity of humanized anti-CD20 monoclonal antibody and polymorphism in IgG Fc receptor FcγRIIIa gene. *Blood* **99**, 754–758 (2002).
30. W.-K. Weng, R. S. Negrin, P. Lavori, S. J. Horning, Immunoglobulin G Fc Receptor FcγRIIIa 158 V/F polymorphism correlates with rituximab-induced neutropenia after autologous transplantation in patients with non-hodgkin's lymphoma. *J. Clin. Oncol.* **28**, 279–284 (2009).
31. W. Zhang, M. Gordon, A. M. Schultheis, D. Y. Yang, F. Nagashima, M. Azuma, H.-M. Chang, E. Borucka, G. Lurje, A. E. Sherrod, S. Iqbal, S. Groshen, H.-J. Lenz, FCGR2A and FCGR3A polymorphisms associated with clinical outcome of epidermal growth factor receptor–expressing metastatic colorectal cancer patients treated with single-agent cetuximab. *J. Clin. Oncol.* **25**, 3712–3718 (2007).
32. K. Tamura, C. Shimizu, T. Hojo, S. Akashi-Tanaka, T. Kinoshita, K. Yonemori, T. Kouno, N. Katsumata, M. Ando, K. Aogi, F. Koizumi, K. Nishio, Y. Fujiwara, FcγR2A and 3A polymorphisms predict clinical outcome of trastuzumab in both neoadjuvant and metastatic settings in patients with HER2-positive breast cancer. *Ann. Oncol.* **22**, 1302–1307 (2011).
33. L. N. Dahal, C.-Y. Huang, R. J. Stopforth, A. Mead, K. Chan, J. X. Bowater, M. C. Taylor, P. Narang, H. T. C. Chan, J. H. Kim, A. T. Vaughan, F. Forconi, S. A. Beers, Shaving is an epiphenomenon of type I and II anti-CD20-mediated phagocytosis, whereas antigenic modulation limits type I monoclonal antibody efficacy. *J. Immunol.* **201**, 1211–1221 (2018).
34. S. A. Beers, R. R. French, H. T. C. Chan, S. H. Lim, T. C. Jarrett, R. M. Vidal, S. S. Wijayaweera, S. V. Dixon, H. Kim, K. L. Cox, J. P. Kerr, D. A. Johnston, P. W. M. Johnson, J. S. Verbeek, M. J. Glennie, M. S. Cragg, Antigenic modulation limits the efficacy of anti-CD20 antibodies: Implications for antibody selection. *Blood* **115**, 5191–5201 (2010).
35. F. J. Beurskens, M. A. Lindorfer, M. Farooqui, P. V. Beum, P. Engelberts, W. J. M. Mackus, P. W. H. I. Parren, A. Wiestner, R. P. Taylor, Exhaustion of cytotoxic effector systems may limit mAb-based immunotherapy in cancer patients. *J. Immunol.* **188**, 3532–3541 (2012).

36. M. S. Czuczman, S. Olejniczak, A. Gowda, A. Kotowski, A. Binder, H. Kaur, J. Knight, P. Starostik, J. Deans, F. J. Hernandez-Ilizaliturri, Acquirement of rituximab resistance in lymphoma cell lines is associated with both global *CD20* gene and protein down-regulation regulated at the pretranscriptional and posttranscriptional levels. *Clin. Cancer Res.* **14**, 1561–1570 (2008).
37. G. W. Small, H. L. McLeod, K. L. Richards, Analysis of innate and acquired resistance to anti-CD20 antibodies in malignant and nonmalignant B cells. *PeerJ* **1**, e31 (2013).
38. A. Lux, M. Seeling, A. Baerenwaldt, B. Lehmann, I. Schwab, R. Repp, N. Meidenbauer, A. Mackensen, A. Hartmann, G. Heidkamp, D. Dudziak, F. Nimmerjahn, A humanized mouse identifies the bone marrow as a niche with low therapeutic IgG activity. *Cell Rep.* **7**, 236–248 (2014).
39. C. P. Pallasch, I. Leskov, C. J. Braun, D. Vorholt, A. Drake, Y. M. Soto-Feliciano, E. H. Bent, J. Schwamb, B. Iliopoulou, N. Kutsch, N. van Rooijen, L. P. Frenzel, C. M. Wendtner, L. Heukamp, K. A. Kreuzer, M. Hallek, J. Chen, M. T. Hemann, Sensitizing protective tumor microenvironments to antibody-mediated therapy. *Cell* **156**, 590–602 (2014).
40. S. Herter, M. C. Birk, C. Klein, C. Gerdes, P. Umana, M. Bacac, Glycoengineering of therapeutic antibodies enhances monocyte/macrophage-mediated phagocytosis and cytotoxicity. *J. Immunol.* **192**, 2252–2260 (2014).
41. K. Tobinai, C. Klein, N. Oya, G. Fingerle-Rowson, A review of obinutuzumab (GA101), a novel type II anti-CD20 monoclonal antibody, for the treatment of patients with B-cell malignancies. *Adv. Ther.* **34**, 324–356 (2017).
42. E. Mössner, P. Brünker, S. Moser, U. Püntener, C. Schmidt, S. Herter, R. Grau, C. Gerdes, A. Nopora, E. van Puijenbroek, C. Ferrara, P. Sondermann, C. Jäger, P. Strein, G. Fertig, T. Friess, C. Schüll, S. Bauer, J. D. Porto, C. D. Nagro, K. Dabbagh, M. J. S. Dyer, S. Poppema, C. Klein, P. Umaña, Increasing the efficacy of CD20 antibody therapy through the engineering of a new type II anti-CD20 antibody with enhanced direct and immune effector cell–mediated B-cell cytotoxicity. *Blood* **115**, 4393–4402 (2010).
43. M. Feng, W. Jiang, B. Y. S. Kim, C. C. Zhang, Y.-X. Fu, I. L. Weissman, Phagocytosis checkpoints as new targets for cancer immunotherapy. *Nat. Rev. Cancer* **19**, 568–586 (2019).
44. K. Nakamura, M. Casey, H. Oey, F. Vari, J. Stagg, M. K. Gandhi, M. J. Smyth, Targeting an adenosine-mediated "don't eat me signal" augments anti-lymphoma immunity by anti-CD20 monoclonal antibody. *Leukemia* **34**, 2708–2721 (2020).
45. M. P. Chao, A. A. Alizadeh, C. Tang, J. H. Myklebust, B. Varghese, S. Gill, M. Jan, A. C. Cha, C. K. Chan, B. T. Tan, C. Y. Park, F. Zhao, H. E. Kohrt, R. Malumbres, J. Briones, R. D. Gascoyne, I. S. Lossos, R. Levy, I. L. Weissman, R. Majeti, Anti-CD47 antibody synergizes with rituximab to promote phagocytosis and eradicate non-hodgkin lymphoma. *Cell* **142**, 699–713 (2010).
46. A. A. Barkal, R. E. Brewer, M. Markovic, M. Kowarsky, S. A. Barkal, B. W. Zaro, V. Krishnan, J. Hatakeyama, O. Dorigo, L. J. Barkal, I. L. Weissman, CD24 signalling through macrophage Siglec-10 is a target for cancer immunotherapy. *Nature* **572**, 392–396 (2019).
47. A. W. Harris, C. A. Pinkert, M. Crawford, W. Y. Langdon, R. L. Brinster, J. M. Adams, The E mu-myc transgenic mouse. A model for high-incidence spontaneous lymphoma and leukemia of early B cells. *J. Exp. Med.* **167**, 353–371 (1988).
48. D. Michonneau, P. Sagoo, B. Breart, Z. Garcia, S. Celli, P. Bousso, The PD-1 axis enforces an anatomical segregation of CTL activity that creates tumor niches after allogeneic hematopoietic stem cell transplantation. *Immunity* **44**, 143–154 (2016).
49. B. Young, R. Wightman, R. Blanvillain, S. B. Purcel, P. Gallois, pH-sensitivity of YFP provides an intracellular indicator of programmed cell death. *Plant Methods* **6**, 27 (2010).
50. B. Breart, F. Lemaître, S. Celli, P. Bousso, Two-photon imaging of intratumoral CD8$^+$ T cell cytotoxic activity during adoptive T cell therapy in mice. *J. Clin. Investig.* **118**, 1390–1397 (2008).
51. M. Cazaux, C. L. Grandjean, F. Lemaître, Z. Garcia, R. J. Beck, I. Milo, J. Postat, J. B. Beltman, E. J. Cheadle, P. Bousso, Single-cell imaging of CAR T cell activity in vivo reveals extensive functional and anatomical heterogeneity. *J. Exp. Med.* **216**, 1038–1049 (2019).
52. A. K. Church, K. R. Vandermeid, N. A. Baig, A. M. Baran, T. E. Witzig, G. S. Nowakowski, C. S. Zent, Anti-CD20 monoclonal antibody-dependent phagocytosis of chronic lymphocytic leukaemia cells by autologous macrophages. *Clin. Exp. Immunol.* **183**, 90–101 (2016).
53. C. Kerntke, F. Nimmerjahn, M. Biburger, There is (scientific) strength in numbers: A comprehensive quantitation of Fc gamma receptor numbers on human and murine peripheral blood leukocytes. *Front. Immunol.* **11**, 118 (2020).
54. M. B. Overdijk, S. Verploegen, A. Ortiz Buijsse, T. Vink, J. H. W. Leusen, W. K. Bleeker, P. W. H. I. Parren, Crosstalk between human IgG isotypes and murine effector cells. *J. Immunol.* **189**, 3430–3438 (2012).
55. M. Boulch, C. L. Grandjean, M. Cazaux, P. Bousso, Tumor immunosurveillance and immunotherapies: A fresh look from intravital imaging. *Trends Immunol.* **40**, 1022–1034 (2019).
56. P. Bousso, H. D. Moreau, Functional immunoimaging: The revolution continues. *Nat. Rev. Immunol.* **12**, 858–864 (2012).
57. J. J. Pinney, F. Rivera-Escalera, C. C. Chu, H. E. Whitehead, K. R. Van DerMeid, A. M. Nelson, M. C. Barbeau, C. S. Zent, M. R. Elliott, Macrophage hypophagia as a mechanism of innate immune exhaustion in mAb-induced cell clearance. *Blood* **136**, 2065–2079 (2020).
58. D. Daydé, D. Ternant, M. Ohresser, S. Lerondel, S. Pesnel, H. Watier, A. Le Pape, P. Bardos, G. Paintaud, G. Cartron, Tumor burden influences exposure and response to rituximab: Pharmacokinetic-pharmacodynamic modeling using a syngeneic bioluminescent murine model expressing human CD20. *Blood* **113**, 3765–3772 (2009).
59. M. Taskinen, M.-L. Karjalainen-Lindsberg, H. Nyman, L.-M. Eerola, S. Leppä, A high tumor-associated macrophage content predicts favorable outcome in follicular lymphoma patients treated with rituximab and cyclophosphamide-doxorubicin-vincristine-prednisone. *Clin. Cancer Res.* **13**, 5784–5789 (2007).
60. S. Fafi-Kremer, T. Bruel, Y. Madec, R. Grant, L. Tondeur, L. Grzelak, I. Staropoli, F. Anna, P. Souque, S. Fernandes-Pellerin, N. Jolly, C. Renaudat, M.-N. Ungeheuer, C. Schmidt-Mutter, N. Collongues, A. Bolle, A. Velay, N. Lefebvre, M. Mielcarek, N. Meyer, D. Rey, P. Charneau, B. Hoen, J. De Seze, O. Schwartz, A. Fontanet, Serologic responses to SARS-CoV-2 infection among hospital staff with mild disease in eastern France. *EBioMedicine* **59**, 102915 (2020).

Acknowledgments: We thank members of the Bousso laboratory for critical review of the manuscript. We acknowledge the mouse facility and CB UTechS at Institut Pasteur for support in conducting this study. **Funding:** The work was supported by Institut Pasteur, Inserm, and an Advanced grant (ENLIGHTEN) from the European Research Council (P.B.). **Author contributions:** C.L.G., Z.G., F.L., and B.B. conducted the experiments. C.L.G. and P.B. designed the experiments. C.L.G. and P.B. analyzed the data and wrote the manuscript. **Competing interests:** The authors declare that they have no competing interests. **Data and materials availability:** All data needed to evaluate the conclusions in the paper are present in the paper and/or the Supplementary Materials. Additional data related to this paper may be requested from the authors.

Submitted 1 July 2020
Accepted 31 December 2020
Published 19 February 2021
10.1126/sciadv.abd6167

Citation: C. L. Grandjean, Z. Garcia, F. Lemaître, B. Bréart, P. Bousso, Imaging the mechanisms of anti-CD20 therapy in vivo uncovers spatiotemporal bottlenecks in antibody-dependent phagocytosis. *Sci. Adv.* **7**, eabd6167 (2021).

Science Advances

Imaging the mechanisms of anti-CD20 therapy in vivo uncovers spatiotemporal bottlenecks in antibody-dependent phagocytosis

Capucine L. Grandjean, Zacarias Garcia, Fabrice Lemaître, Béatrice Bréart and Philippe Bousso

Sci Adv **7** (8), eabd6167.
DOI: 10.1126/sciadv.abd6167

Science Advances (ISSN 2375-2548) is published by the American Association for the Advancement of Science, 1200 New York Avenue NW, Washington, DC 20005. The title *Science Advances* is a registered trademark of AAAS.